

Article

Numerical Simulation of Corrugated Steel Concrete Prefabricated Support Structure for Underground Engineering

Caixia Guo ^{1,*}, Zuozhen Wang ¹, Hongbing Zhao ², Zhiqiang Zhou ² and Miao Wang ²

¹ Institute of Geotechnical and Underground Engineering, Beijing University of Technology, Beijing 100124, China; wangzz97@emails.bjut.edu.cn

² China Railway 22nd Bureau Group Electrification Engineering Co., Ltd., Beijing 102300, China; mingshi99sci@163.com (H.Z.); zhizhou_12@163.com (Z.Z.); wangmiao_305@163.com (M.W.)

* Correspondence: guocaixia@bjut.edu.cn

Abstract: The spray anchor system is commonly used for primary support in underground projects due to its advantages such as fast closure of excavation surfaces, tight connection with the surrounding rock, and high early strength. However, this system has several drawbacks, such as severe pollution, poor working conditions, long construction periods, and high labor costs. In response to the concepts of green construction and prefabrication, this study proposes an innovative composite structure consisting of corrugated steel plates and concrete, namely, corrugated steel–concrete (CSC), which is a prefabricated support structure for underground engineering. The proposed system involves on-site corrugated steel plates and concrete, and the concrete is poured into the corrugated steel plates without using shotcrete. This approach mitigates pollution and improves working conditions. After the introduction to the novel structural system, elaborate Abaqus numerical models are developed to investigate the mechanical performance considering full elastoplastic response until failure. The steel–concrete interfacial connections, as a major factor in composite structures, are carefully studied and discussed based on the delicate interfacial contact model. The deformations, stress distributions, and failure types are analyzed. A parametric analysis is also conducted to expand the efficient range. Theoretical analysis is further carried out, and design expressions are proposed, which are verified to be suitable for design considerations.



Citation: Guo, C.; Wang, Z.; Zhao, H.; Zhou, Z.; Wang, M. Numerical Simulation of Corrugated Steel Concrete Prefabricated Support Structure for Underground Engineering. *Sustainability* **2023**, *15*, 14495. <https://doi.org/10.3390/su151914495>

Academic Editor: Xiaojun Feng

Received: 27 July 2023

Revised: 6 September 2023

Accepted: 11 September 2023

Published: 5 October 2023

Keywords: corrugated steel plate; prefabricated support structure; underground engineering; primary support; numerical method

1. Introduction

The rapid growth of modern cities has led to issues of traffic congestion and insufficient land resources. Developing underground urban spaces can be an effective solution to these problems by transferring urban functions underground and reducing the environmental impact on surface spaces. However, underground engineering faces challenges due to limited land resources and the mutual influences of existing buildings [1]. Moreover, as underground engineering significantly affects the environment, the adoption of green and sustainable technologies is crucial for the development of modern cities [2].

The spray anchor construction system, comprising grating/shaped steel arch frame, rebar mesh, and shotcrete, is commonly employed for primary support in underground engineering, offering several advantages such as fast excavation surface closure, high early stage strength, and a tight connection with the surrounding rock [3–5]. However, shotcrete, a crucial component of this system, is not structurally sound and is prone to cracking, leading to potential water leakage. Moreover, the construction technology of this method poses several challenges, including significant environmental pollution, large injection rebound, low efficiency, and high cost [6]. Consequently, shotcrete is not preferred in several countries due to its high levels of pollution. Therefore, there is a pressing need for a



Copyright: © 2023 by the authors. Licensee MDPI, Basel, Switzerland. This article is an open access article distributed under the terms and conditions of the Creative Commons Attribution (CC BY) license (<https://creativecommons.org/licenses/by/4.0/>).

novel form of underground support system that meets the engineering requirements of green construction, low cost, high efficiency, high performance, mechanizability, flexibility, and safety.

The increasing demand for underground construction necessitates the development of new support systems. Some scholars use geopolymer concrete as an eco-friendly approach for tunnel lining [7,8]. This study proposes an innovative composite structure consisting of corrugated steel plates and concrete, namely, corrugated steel–concrete (CSC), which is a prefabricated support structure for underground engineering. The case of tunnel primary support is considered in this paper, considering the non-uniform distributed load and the interaction with the surrounding rock. The proposed system is also suitable for underground lining.

The CSC composite structure offers significant advantages. Firstly, the high ductility of steel endows the corrugated steel plate with good tensile properties, allowing for large deformation of the surrounding rock, particularly when the surrounding rock is weak [9]. Secondly, the corrugated steel plate can be prefabricated in the factory and assembled on-site, enhancing construction efficiency [10]. Most importantly, the absence of shotcrete renders the construction process environmentally friendly and operationally improved [11].

The application of assembled corrugated steel plate structures as primary support in underground projects has been proposed [12]. The feasibility and effectiveness of using corrugated steel plate for the strengthening of existing underground projects were analyzed, demonstrating that corrugated steel plate lining is capable of preventing the lining from falling [13]. Previous research employed corrugated plates as a trial for repairing tunnels [14]. The mechanical behavior of the interaction between surrounding rock and corrugated steel plates has been investigated [15]. Additionally, the impact of the underground environment and construction process on the corrosion risk of rusted corrugated steel plates has been studied [16]. The mechanical properties of buried corrugated pipes under dynamic loads have been analyzed [17–19]. Recently, a new type of corrugated steel plate structure was proposed as the primary support in tunnels, and its capacity was evaluated using ANSYS finite element software [20,21]. The differences in prefabricated corrugated steel primary support structures, constructed using various methods, were studied through monitoring and simulation [19].

Numerous studies have been conducted on the mechanical performance of corrugated steel plates in shear walls [22], including the use of novel materials [23] and the investigation of dynamic responses [24,25]. Similar research has also been performed on underground pipes or tunnels that use stiffened steel plates [26]. The application of composite slabs or beams using concrete and corrugated steel plates in buildings and bridges has been investigated [27,28]. For large-scale tunnel engineering, steel plate–concrete composite structures have been proposed and studied in recent years [29–31].

The use of concrete connected to corrugated steel plates as load-bearing structures has also been widely adopted in pipelines, culverts, and tunnel strengthening [32,33]. Steel frame–concrete initial supports for tunnels have also been studied, while research has explored the connections between these two different materials [34,35]. The feasibility of the proposed construction method has been verified through tests, while theoretical analyses and three-dimensional numerical simulations have been conducted to investigate the key parameters involved in assembled corrugated steel plate structures.

Several studies have investigated the mechanical performance of corrugated steel plates and corrugated steel–concrete composite beams/slabs in various applications such as shear walls, bridges, and road embankments [9,36,37]. However, limited studies have been conducted on the application of corrugated steel plates as composite structures with concrete as the primary support. Pure steel structures have been found to have issues with connections to the surrounding rock, large gaps, and high costs, among others. To address this, a novel structural system is proposed in this paper, known as the CSC composite structure. This system involves the fabrication of corrugated steel plate segments in a factory, which are then assembled on-site using bolt connections. Concrete is then poured

into the corrugated steel plate to form the composite structure. This support system offers advantages such as low pollution, fast construction, small size, high capacity, low cost, and no gaps. With all structure members prefabricated in the factory, on-site assembly and concrete casting are the only required procedures. Moreover, it is essential to emphasize the broader socio-economic benefits of this innovative approach. By offering enhanced environmental sustainability and safety, the corrugated steel–concrete prefabricated support structure not only contributes to a more responsible and secure underground construction industry, but also carries significant economic advantages. These benefits can include reduced maintenance and repair costs, faster project completion times, and improved resource utilization. After the introduction to the novel system, numerical and theoretical analyses are carried out to investigate the mechanical performance of the proposed structure, including elastoplastic response and parametric analyses. Finally, design expressions are proposed for practice. The results demonstrate that the proposed structure offers superior mechanical and construction performances, making it a promising choice for tunnel primary support and lining in future projects. The objective of this study is to investigate the lateral load-bearing performance of the corrugated steel–concrete prefabricated support structure, establish numerical and theoretical models, and propose design methods for engineering reference.

2. Structural Design

2.1. Main Structure

The CSC composite structure system is developed for tunnel primary support, which can avoid the usage of shotcrete, and solve the problems of pure steel support systems including structural gaps, casting leakage, and loose connections. A CSC support system consists of two main parts: a corrugated steel plate, and concrete (in the corrugated steel plate). The corrugated steel plate manufactured in the factory in segments is assembled on-site. The concrete is poured into the corrugated steel plate on site.

2.2. Corrugated Steel Plate

A corrugated steel plate segment, as demonstrated in Figure 1, contains multiple components such as a corrugated panel, two side flanges, two end flanges, several preserved bolt holes, a preserved pipe hole for concrete pouring, and another preserved pipe hole for pressure control. It is noteworthy that the side and end flanges serve as central connecting components in both directions, and the preserved bolt holes are evenly arranged in the flanges to facilitate positioning and connections during the assembling process. The height of the segment, represented by H , can be determined based on the excavation step level. The flange widths, expressed as B_1 and B_2 , should satisfy the requirements for bolt connection. Furthermore, the arc length, designated as L , should be based on the inner diameter of the supporting structure, and consider various factors such as the number of lateral assembling segments, self-weight, and assembling and construction feasibilities.

In accordance with Figure 2, the essential geometric parameters of the corrugated plate include the wave width denoted as w , the steel height represented by h_s , the steel thickness designated as t_s , and the concrete height/thickness expressed as h_c . To streamline the production process, standardized dimensions of corrugated steel plates, which are readily available on the market [38], may be adopted in compliance with local codifications. Nevertheless, customized dimensions tailored to specific cases may be preferred to satisfy technical requirements. Furthermore, the material design must conform to the principles of steel–concrete composite structures in accordance with codes [39].

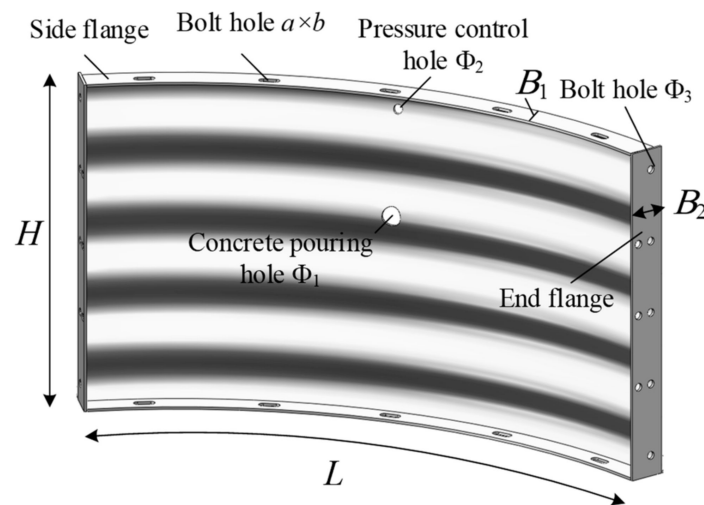


Figure 1. Design of corrugated steel plate segment.

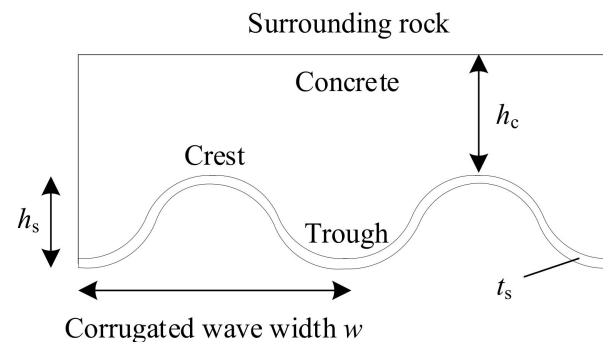


Figure 2. Corrugated steel plate dimensions.

2.3. Structural Characteristics

The proposed CSC composite structure exhibits several distinct characteristics with regard to its structural performance. Firstly, casting pressure applied during concrete pouring compacts the surrounding rock, enhancing its density. Furthermore, uneven surfaces between the rock, corrugated steel panel, and the concrete fortify mutual connections, ultimately improving structural performance through composite actions between the steel, concrete, and surrounding rock. Secondly, the flanges present in the corrugated steel segment act as connectors between the steel and concrete, further augmenting the composite effect while meeting full composite condition requirements under most load cases, owing to the uneven surface and interfacial friction that are involved. Thirdly, the utilization of bolts in the assembly and the filling of the corrugated steel plate with concrete significantly reduces environmental pollution while greatly improving construction efficiency. This structurally versatile design can be employed as primary support, permanent support, or temporary support based on the project requirements.

However, several practical considerations must be kept in mind: (a) temporary braces may need to be utilized to stabilize the steel plate during concrete casting operations to withstand deformation caused by casting pressure, particularly in larger-scaled projects; (b) additional interfacial connectors may be required for special load cases characterized by significant shear forces in the steel–concrete interfaces; (c) surface enhancement and anti-permeability performances may not be as robust as in shotcrete applications, which should be duly considered in structural design.

3. Numerical Modeling

3.1. General Setting

Abaqus is widely used software for finite element analysis and computer-aided engineering simulations. It employs advanced numerical methods and algorithms, allowing it to provide highly accurate simulation results. Due to its capability to handle complex engineering structural systems, extensive material modeling options, and excellent customizability and extensibility, this study utilizes Abaqus for detailed numerical simulations. As shown in Figure 3, shell element (S4R) is used for corrugated steel plate, while solid element (C3D8R) is used for concrete. Although it was found that the beam model was, to some extent, equivalent to the shell-based elaborate model and could improve efficiency [20], one of the key targets in this research is to investigate the properties and influences of the steel–concrete interface; thus, the beam model is not appropriate here due to the lack of interfacial details. Node-to-surface contact pairs are set in the steel–concrete interfaces, which have properties of: normal hard contact that the slave nodes cannot penetrate the master surface; tangential penalty friction, which follows the Mohr–Coulomb law; and cohesive behaviors both in the normal and tangential directions. The details of the interface model will be discussed in the following sections.

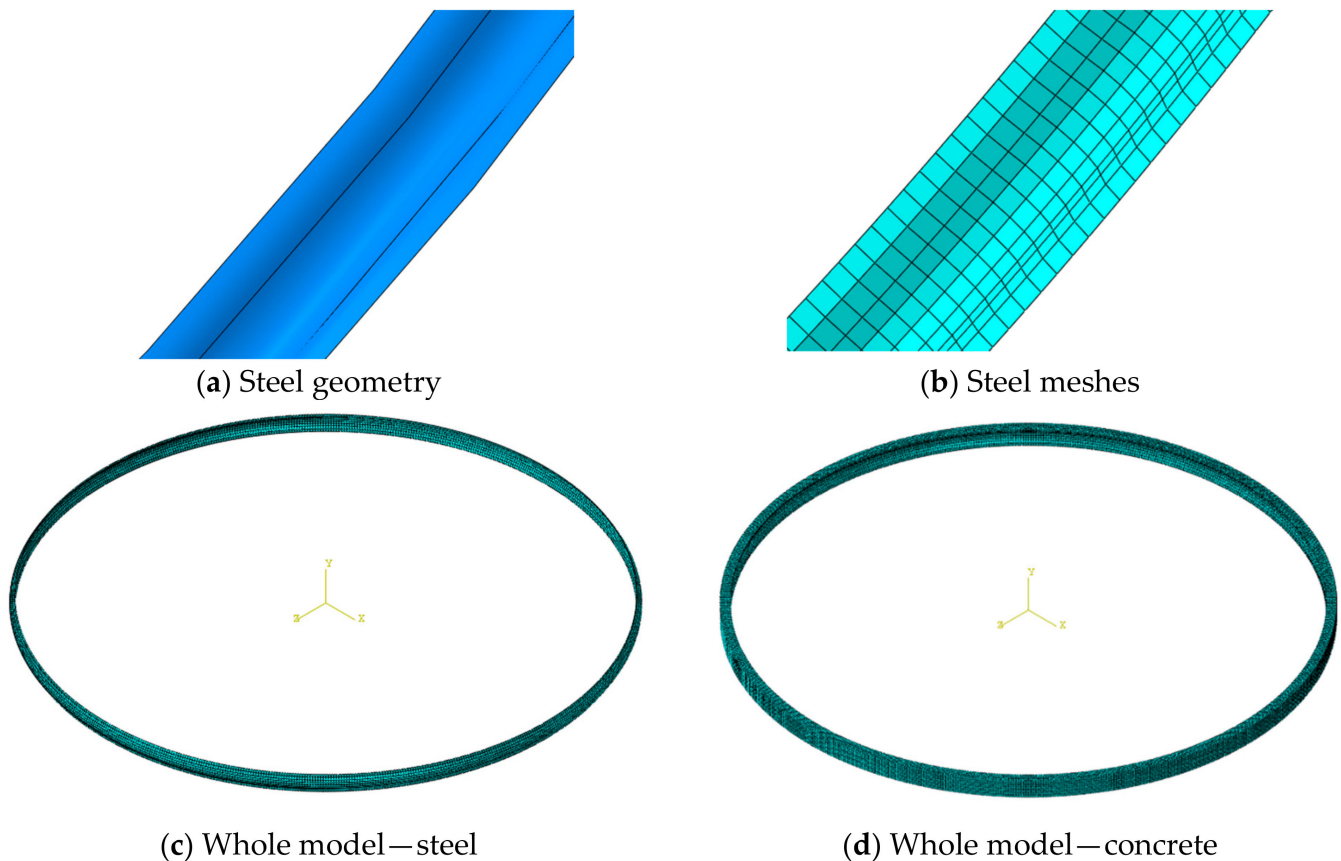


Figure 3. Elements and meshes.

In the tunnel's longitudinal direction, a full wave (a length of w) of the corrugated plate, as shown in Figure 2, is built in the model due to symmetry and to save costs. The shape of the corrugated plate follows the Chinese Code for Design of Railway Tunnel [38] and the basic model uses the parameters $w = 200$ mm, $h_s = 50$ mm. The thickness of the outer concrete is considered as $h_c = 50$ mm in the basic model, noting that this is the distance from the outer crest of the corrugated plate.

A global mesh size of 25 mm (about 8–10 elements along a full wave of the corrugated plate) is used in the model, which is representative of the geometry and gives enough accuracy.

3.2. Boundary Conditions and Loads

The soil foundation interaction is also modeled by solid elements and interaction. An elastic foundation assumes that the soil uses an elastic C3D8R element with a modulus and thickness giving an equivalent foundation stiffness of $k_{\text{soil}} = 150 \text{ MPa/m}$. This foundation stiffness value is similar to previous studies on pure steel corrugated tunnel supports [20] and is a relatively small value considering soft surrounding rocks. Firmer surrounding rocks with higher k_{soil} will yield smaller deformation and stress results, thus leading to less conservative results. By utilizing a basically lower boundary value, the results in this research are on the safe side. The boundary conditions for the whole section are considered in the model, as shown in Figure 4. Contact is also set in the soil–concrete interface using only normal hard contact; thus, only compression effects could exist in the soil–concrete interface and the tangential direction is frictionless. According to the literature, it is reasonable to ignore part of the top boundary to improve efficiency. However, this simplification needs pre-estimation of areas in contact that are dependent on the load pattern. In this research, since compression-only contact is set between the tunnel and the soil, the natural boundary conditions are met and are more accurate as the contact regions are calculated by the model. Also, considering the longitudinal symmetry, the out-of-plane deformation is constrained in the model.

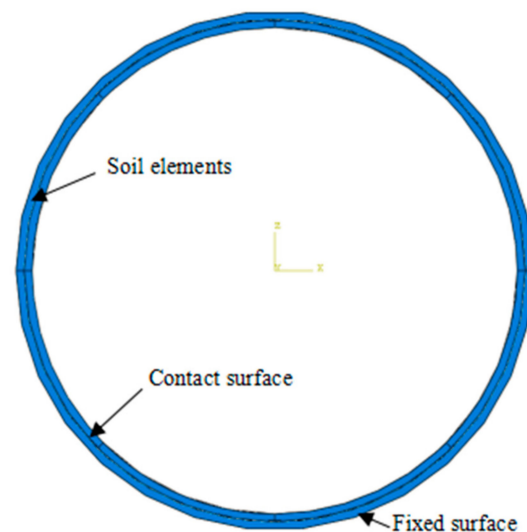
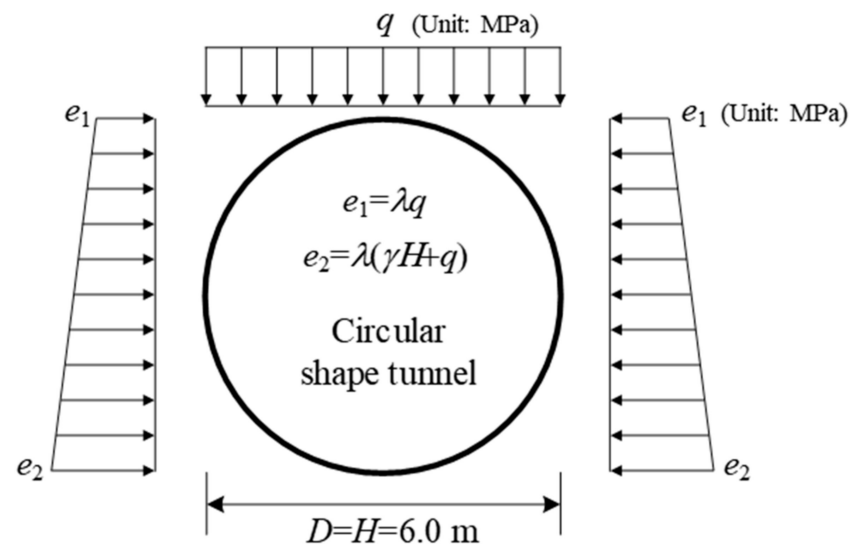
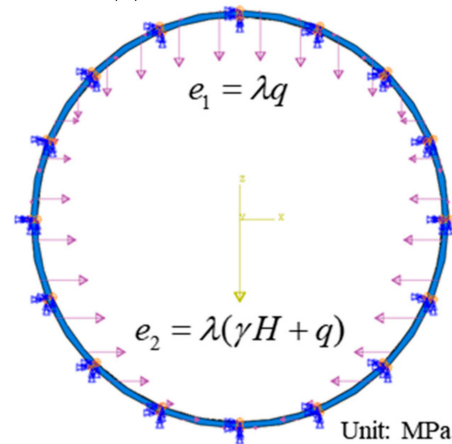


Figure 4. Boundary condition modeling of the compression-only elastic soil foundations.

The typical load patterns are used as shown in Figure 5. The top pressure q is derived from the soil weight and tunnel depth. A general soil unit weight $\gamma = 20 \text{ kN/m}^3$ is considered and a ground overload $q_0 = 20 \text{ kN/m}^2$ is also taken into account, which is equivalent to a 1m soil depth. The lateral pressure coefficient used is 0.40. By utilizing different q , loads representing different depths can be simulated. Also, structural gravity is considered, giving an acceleration of 9.8 m/s^2 and a material weight of 25 kN/m^3 and 78 kN/m^3 for concrete and steel, respectively. To simulate the non-uniform load distribution, the surface traction type load is applied with the analytical field tool. Note that the applied load only acts in a projective way to its direction, while Abaqus, by default, considers the whole area of the inclined surface (not considering direction); thus, this non-perpendicular effect is considered in the formulation of the analytical field.



(a) Load definition



(b) Load applied in the FEM

Figure 5. Typical load patterns of circular-shaped tunnel.

3.3. Materials

As shown in Figure 6, the concrete damage plasticity (CDP) model is adopted. The compressive and tensile curves of Mode Code [40] are used, while the descending curve of the concrete is taken as a linear form suggested by Hognestad [41]. Concrete class C30 is considered in the basic model. A steel strength of 345 MPa is used in the basic model with the idea of plasticity; thus, strain hardening is not involved, which is consistent with typical code provisions.

Basic concrete plastic parameters are adopted with a dilation angle $\phi = 10^\circ$, eccentricity $\epsilon = 0.1$, yield surface shape $K_c = 0.667$, the ratio between the biaxial and uniaxial compressive strength as $f_{\text{bia}}/f_{\text{uni}} = 1.16$, and the viscosity parameter 0.001. Since this basically monotonic loading and the strain distribution is relatively uniform, damage parameters are not set in the model. Trials were conducted to test the differences using concrete damage parameters of $d = 1 - \sigma/\sigma_u$ [42], and no significant effects were observed.

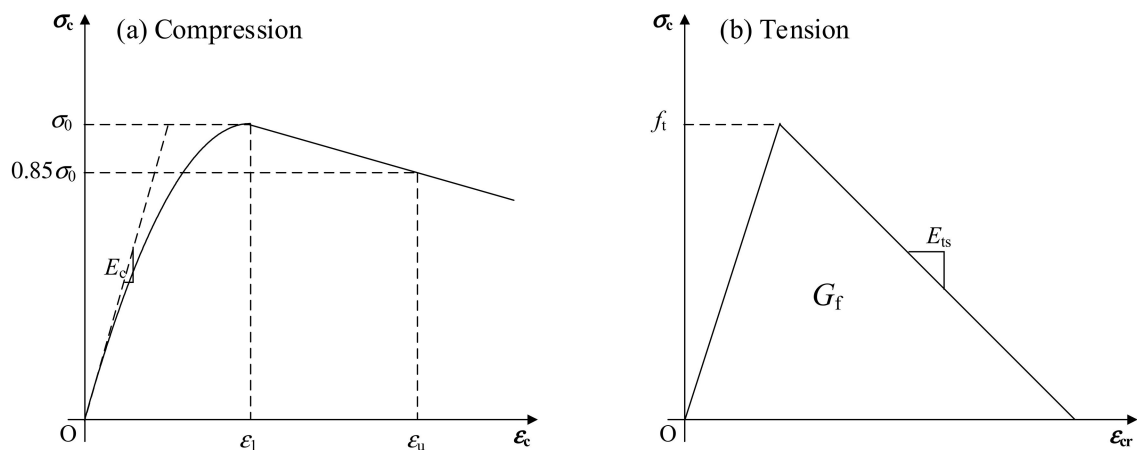


Figure 6. Constitutive curves of CDP concrete.

3.4. Interfaces

The constitutive curves of the interface model are shown in Figure 7. The mechanical properties of the interface involve normal contact, tangential friction, and cohesion (both in normal and tangential directions) [29,42]. “Hard contact” is set in the normal direction, and penalty friction with a coefficient of 0.5 is set in the tangential direction. Cohesive behavior is more complex than normal contact or tangential friction. However, cohesive properties are required in the interface to simulate possible normal and tangential bonds. For the elastic part, the normal and tangential stiffnesses were given as $K_{nn} = 100 \text{ N/mm}^3$ and $K_{ss} = K_{tt} = 30 \text{ N/mm}^3$, which are derived from elastic theory [43]. It is found in this study that the overall behavior is not sensitive to K_{nn} or K_{ss}/K_{tt} . For the plastic behavior, a damage initiation criterion and a damage evolution criterion should be defined. As there are not enough clues about the bond stress between the film bag and the steel plate, this stress is considered as being between 0 MPa (no cohesion) and 0.2 MPa to investigate its influence. As for cohesive damage evolution, a linear descending form is taken, as no obvious influence is found between the exponential form. An ultimate displacement 1.0 mm is used.

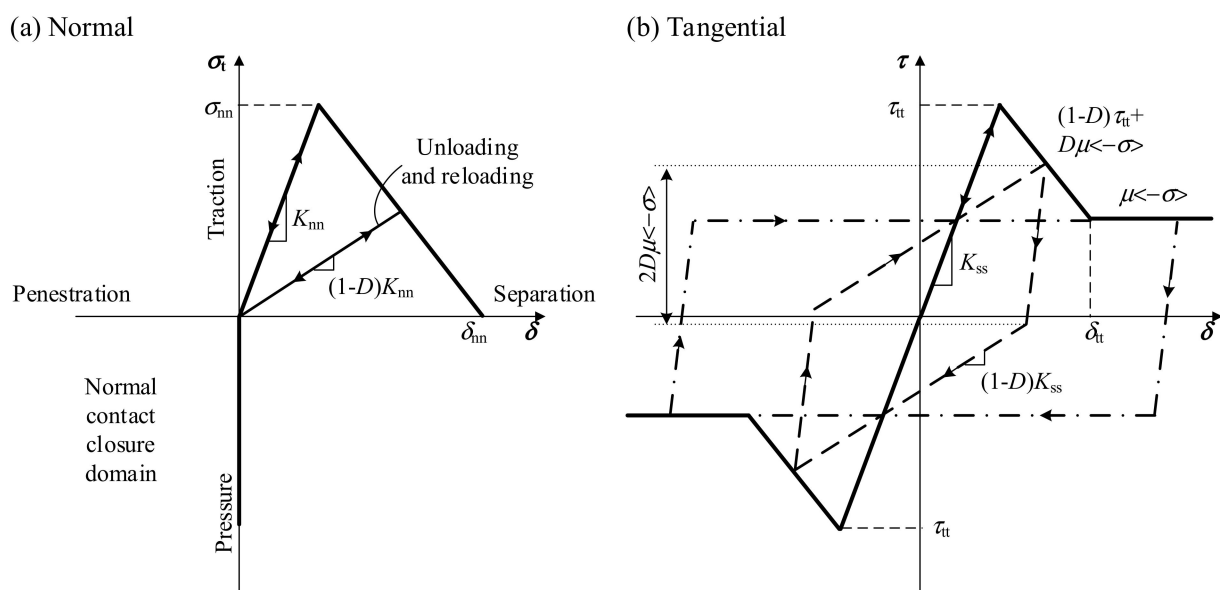


Figure 7. Constitutive curves of the interface model [44].

In the realm of inter-surface interaction, the compressive behavior between surfaces in the contact normal direction is governed by the pressure overclosure relationship independently of the cohesive behavior, due to differences in the contact regime involved. Specifically, the pressure overclosure relationship applies when a slave node interacts with the master surface, while the cohesive behavior contributes to the contact normal stress exclusively when a slave node is not in contact. Conversely, in the shear direction, provided that the cohesive stiffness endures no damage, it is assumed that the cohesive model is active and the friction model remains latent. During tangential slip, which is regarded as entirely elastic, the cohesive strength of the bond resists the slippage and gives rise to shear forces. When damage has been established, the cohesive bond's contribution to the shear stresses initiates a process of degradation. With the associated reduction in cohesive stiffness, the friction model becomes engaged and assists in producing shear stresses. The magnitude of the elastic stick stiffness in the friction model is increased proportionally to that of the elastic cohesive stiffness undergoing degradation. Before the complete failure of the cohesive bond, and subsequent to its initial degradation, the shear stress results from a combination of both the cohesive and frictional contributions. After reaching maximum degradation, the cohesive bond's contribution to the shear stresses becomes null, leaving the friction model as the sole contributor.

4. Results and Discussion

4.1. Influence of Interfacial Bond

Applying $q = \gamma H + q_0 = 200 \text{ kN/m}^2$, representing a soil depth of $H = 9 \text{ m}$, the results are compared as below. As a lower boundary, the interface without cohesion is chosen as the basic model. As shown in Figure 8, the overall structure deforms downwards with a maximum deflection of 12.36 mm in the middle top and a minimum deflection of 1.93 mm in the middle bottom. In the transverse direction, it is found that the lateral foundation offers consideration reaction since a maximum displacement of 3.32 mm exists. This lateral displacement indicates that it is reasonable and necessary to consider a wide range of boundaries in the model. As shown in Figure 9, both for steel and concrete, the maximum stress typically exists in the middle top as compression stress. In this case, without cohesion, the maximum stress in steel is $-85.76/+11.58 \text{ MPa}$ for compression/tension, respectively, while those for concrete are $-12.87/+2.08 \text{ MPa}$. The tensile stress for steel is generally very small. As for the concrete tension, the region is close to the steel plate and wrapped by the plastic bag, leading to an ignorable cracking influence.

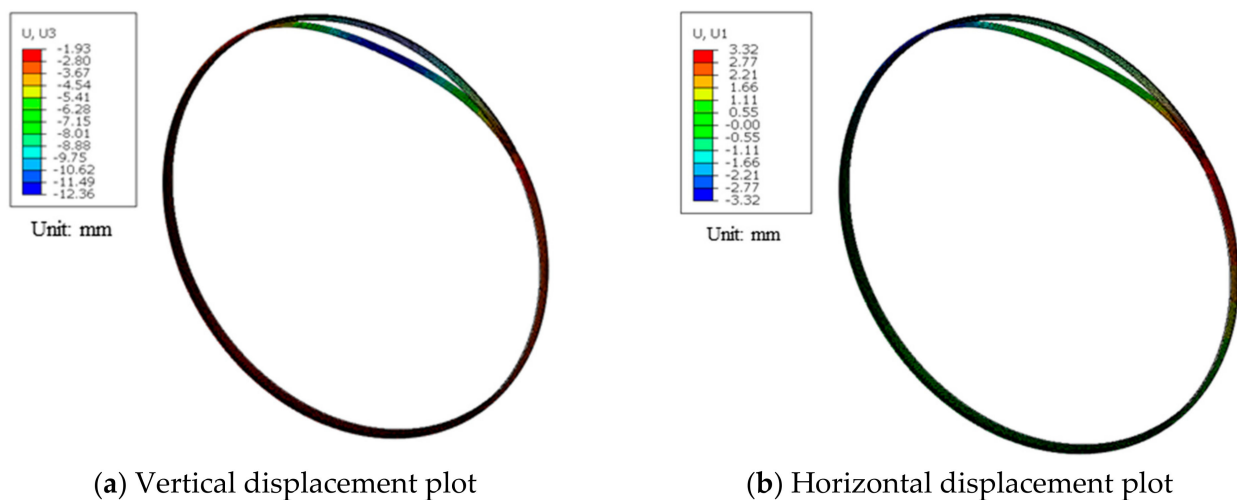


Figure 8. Deformations of the basic model.

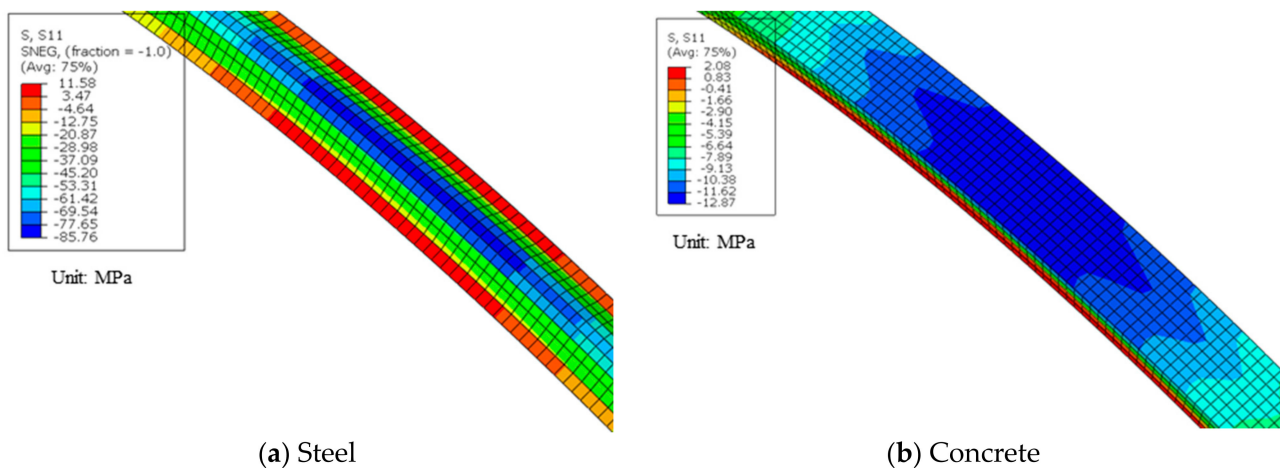


Figure 9. Stress in the circular direction.

Similarly, considering a cohesive bond stress of 0.2 MPa, the maximum steel stress and concrete stress are $-77.55/+28.43$ MPa and -13.31 MPa/ $+2.04$ MPa, respectively, and deflections at the top/bottom of $-10.89/-1.91$ mm, respectively. Further, considering the full bond case for a full composite structure, the interfacial tie technique is used between steel and concrete instead of contact, which constrains all of the freedoms together and prohibits slip. The relative results yield steel and concrete stresses of $-78.30/+29.75$ MPa and $-13.32/+1.98$ MPa, respectively, and deflections at the top/bottom of $-10.75/-1.91$ mm, respectively. Through comparisons, it is found that when only frictions are considered, the maximum deflection at the top increases by 19.7%; however, when considering a small tangential cohesive stress of 0.2 MPa, this increase changes to 1.3%, which is basically the same as the full bond case. Similar impacts of interfacial bonds exist for stress. When there is friction alone, the maximum steel stress (in compression) increases by 9.5%; a 0.2 MPa cohesive stress basically yields the same results as the full bond case. Concrete stress, on the other hand, demonstrates a decreasing trend when the interfacial bond is weaker, but the varying amplitude is small (in the above case within 5%).

The above results suggest that interfacial slip does influence the mechanical behaviors, but to a limited extent. The slip mainly occurs in the initial stage when the normal contact stress and the associated frictional stress are marginal; thus, a small initial bond stress (cohesive stress) could prohibit the slip and yield similar results to the full bond case. For safety considerations, the following analyses use the friction-only interfacial model with initial slippage, which will yield lower boundary results. However, in a simplified design, a full-bond condition could be assumed and reduction factors of 0.8/0.9 could be adopted for deformation and stress, respectively.

4.2. Ultimate Response

In the above analyses, it can be seen that when $q = 200$ kN/m² (soil depth $H = 9$ m), the structure is still in an elastic range. Therefore, the loads are gradually increased to investigate the structural responses. Since variable q will change e_1 and e_2 according to Figure 5, the ratio between e_1 and e_2 also changes in this process and, therefore, the shape of the lateral load is influenced. A two-step loading strategy is used to deal with this issue. In step one, the structure is considered in a zero-depth, and the ground load and lateral load including the component $\lambda\gamma H$ in e_2 are applied. In step two, the depth is gradually increased, and since the load q and λq are only related to the depth, the shape function of the lateral load in this step is constant and, thus, is easy to build.

Figure 10 shows maximum stresses and deflection changing with the loads, in which the concrete stress and deflection are amplified by a factor 3.0 to make them more clear. Von Mises stress is used for steel and concrete, since it is more representative in the

multi-axial stress state. Note that the von Mises stress for concrete is mainly an indicator of concrete compressive stress. It is found that the stress and deformation distributions are similar to those shown in Figures 8 and 9, and the structure fails in the middle span at the top. In Figure 10, it can be seen that the structure has an approximately linear response before steel yielding. The relatively flat initial part is in loading step one, as discussed above. Although the load could further increase after steel yielding, it is out of the typical scope of design. In this study, the elastic limit is defined as the ultimate state. In the case shown in Figure 10, the elastic limit is reached when the steel yields. If the structure has different parameters, it is possible the concrete crushes before the steel yields, and in that case, the concrete crushing is the structure limit.

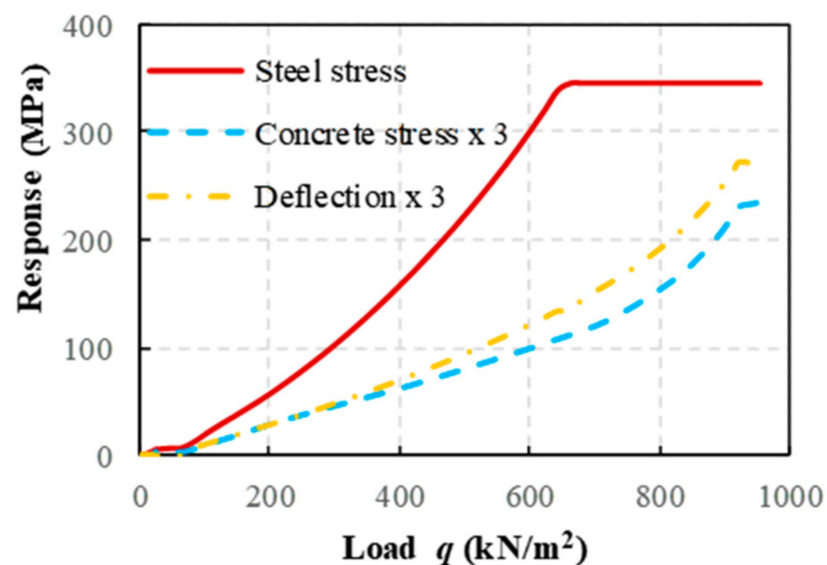


Figure 10. Stresses and deformations increase with loads.

In the basic case shown in Figure 10, when steel stress reaches $f_{sy} = 345$ MPa, $q = 651$ kN/m² corresponds to a soil depth of 31 m. When the material limitation is lower, linear interpolation could be applied to calculate the corresponding allowable load. For example, if the allowable strength of the steel is 210 MPa, the maximum load could be assumed as $651/345 \times 210 = 396$ kN/m². Note that the curves in Figure 10 are actually convex downward, and a linear assumption would give conservative results, which is on the safe side. The elastic design limit criteria could also be used for concrete stress and deflection, and the lower bounds of different design requirements should be met.

5. Parametric Studies

To investigate the influences of different parameters and to give references for practical design, parametric studies were conducted and the results are shown in Table 1. Here, No. 1~No. 12 change the parameters based on the standard case discussed above to investigate the influences, while No. 13~No. 20 choose the parameter from national standards [45] to give references for practical design. In Table 1, the definitions of sectional parameters are consistent with in Figure 3: q_{max} represents the load capacity (at the top of the structural influenced by soil weight and depth) at the ultimate state, σ_s , σ_c and δ_{max} are the corresponding stresses and displacements, and q/δ is the ratio between q_{max} and δ_{max} , representing the concept of stiffness. In Table 1, it can be seen that for most cases, the structures reach the load limit when the steel approaches yield strength. On the opposite side, when the concrete is relatively thick in some cases, the structures reach the limit when the concrete crushes while the steel is still in an elastic state. Note that due to the confinement effect provided by the steel, the concrete crush strength is typically larger than the uniaxial compressive strength and sometimes up to twice that of the uniaxial

strength, which is an obvious advantage of the composite structures. Since concrete crush failure usually occurs when the steel ratio is too small and is very brittle, this failure type is typically suggested to be avoided in design.

Table 1. Results of parametric studies.

No.	Parameters				Results				Prediction		
	w (mm)	h_s (mm)	t_s (mm)	h_c (mm)	q_{max} (kN/m ²)	σ_s (MPa)	σ_c (MPa)	δ_{max} (mm)	q/δ	q_{pre} (kN/m ²)	Err.
1				50	651.1	345.0	37.6	46.5	14.0	663.3	1.9%
2				100	1012.9	345.0	44.4	54.7	18.5	1052.8	3.9%
3			6.0	150	1155.8	230.4	39.7	44.7	25.9	-	-
4				200	1165.9	163.0	33.8	36.6	31.9	-	-
5		50	2.0		526.3	345.0	40.4	45.3	11.6	480.8	-8.7%
6	200		4.0		591.5	345.0	37.0	43.4	13.6	572.0	-3.3%
7			8.0	50	705.9	345.0	37.1	47.6	14.8	754.5	6.9%
8			10.0		757.2	345.0	35.8	47.2	16.0	845.7	11.7%
9		75			1076.7	345.0	38.7	49.5	21.7	1085.1	0.8%
10		100		100	1164.5	339.5	37.2	46.9	24.8	-	-
11	150		6.0		684.2	345.0	39.5	48.3	14.2	683.8	-0.1%
12	250	50		50	656.9	345.0	37.0	47.5	13.8	653.2	-0.6%
13	75	25	4.0	50	545.7	345.0	53.6	53.9	10.1	585.7	7.3%
14	125	25	4.0	50	525.9	345.0	54.1	58.0	9.1	565.3	7.5%
15	150	50	6.0	100	1039.6	345.0	45.4	54.8	19.0	1073.3	3.2%
16	200	55	6.0	100	1019.4	345.0	41.8	52.9	19.3	1058.5	3.8%
17	230	64	6.0	100	1029.0	345.0	40.7	51.4	20.0	1059.2	2.9%
18	300	110	6.0	150	1250.5	295.6	34.4	42.1	29.7	-	-
19	380	140	6.0	150	1409.8	345.0	33.5	45.5	31.0	1472.7	4.5%
20	400	150	6.0	150	1445.1	345.0	34.2	45.8	31.5	1474.6	2.0%
										AVE.	2.7%
										STD.	4.7%

The influences of typical sectional parameters on ultimate load capacities are shown in Figure 11. The data points are chosen from Table 1 and only the target variable kept changing. It can be seen from Figure 11a that the load capacity increases with concrete thickness to a limited extent. As discussed above, if the concrete thickness is too large and not compatible with the steel (too small a steel ratio), the structure will experience brittle failure in concrete crush. Figure 11b,c show that the load capacity increases linearly with steel height and steel thickness, indicating a first-order relationship with the steel area. Figure 11c shows that the load capacity decreases with wave length, but to a limited extent, of which the effect might be ignored. These observations are useful in design consideration.

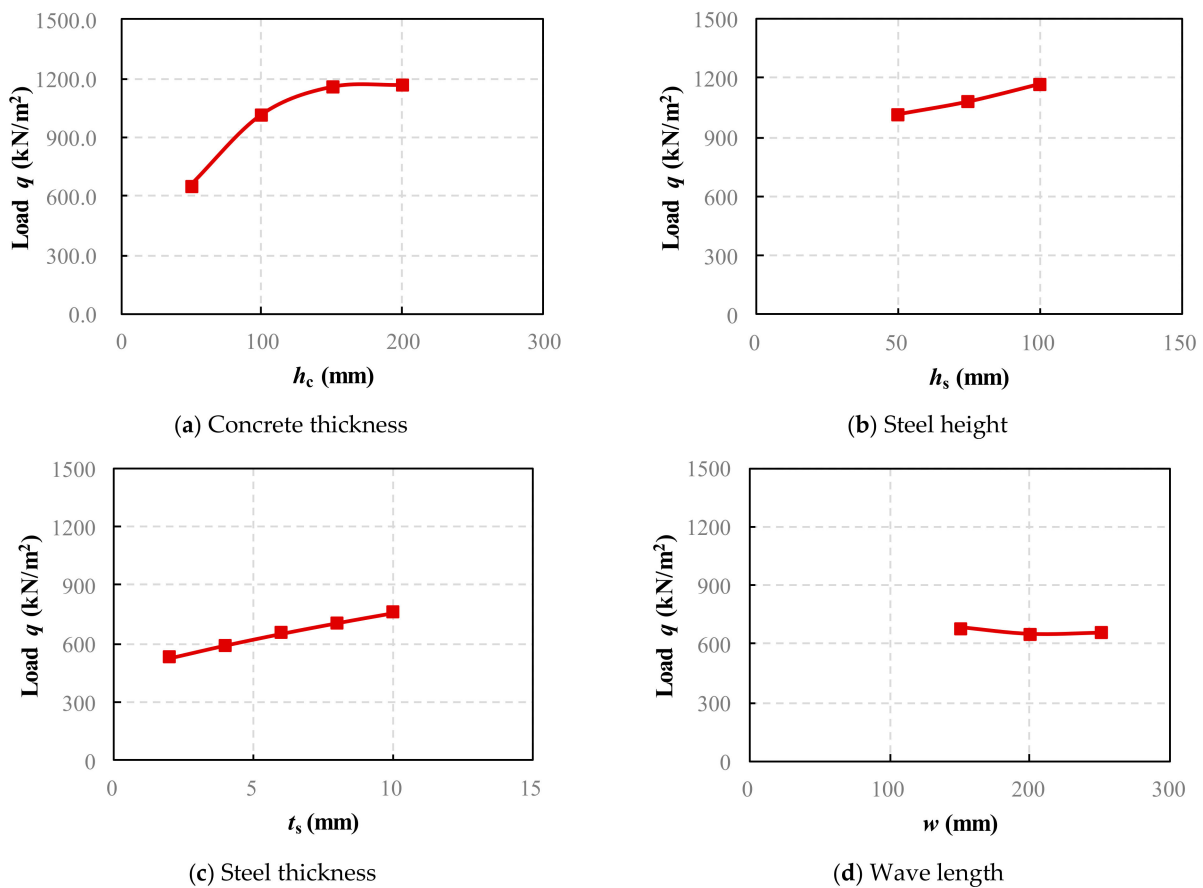


Figure 11. Influences of different parameters on load capacities.

6. Design Considerations

In this section, design considerations are proposed for practice. Based on the numerical observations and parametric analyses, theoretical analyses are carried out for the load capacity, which is the main design target. The structural stiffness, on the other hand, could adopt elastic assumptions and full-bond conditions, as discussed in Section 4.1, and be considered in an elastic model.

As shown in Figures 8 and 9, the deformations and stress distributions of the structure suggest that the middle top area, which is prone to failure, is in a state of compression and bending. Although bending deformation causes the middle top area to deflect downward, the compression is the major effect, as the compressive stress in the steel is much larger than the tensile stress. As shown in Figure 12, the compression force shifts the bending stress to the negative compression side. Since the crest is near the neutral axis, it has the largest compressive stress, and approximately equals the average compressive stress resulting from the sectional compressive force. This can be verified from Figure 9, as the crest has the largest compressive stress, while the trough has low tensile stress. Based on this observation, the ultimate load capacity corresponding the yield of the steel crest could be mainly determined by the sectional compressive force. On the force side, the load causes compressive force and a bending moment in the middle top area. The sectional compressive force is the only variable of concern, as discussed above, and could be roughly assumed based on a uniformly compressed circular ring model:

$$N_{\text{comp}} = \alpha_1 \frac{q w D}{2} \quad (1)$$

where N_{comp} is the sectional compressive force, D is the diameter of the tunnel, and α_1 is a coefficient considering the difference between the real compressive force and the ideal

compressive force, which could be assumed as 0.31 based on the numerical analyses. By transferring the concrete to equivalent steel by E_s/E_c , the efficient sectional area A_e is:

$$A_e = \gamma_s(w^2 + 4h_s^2)^{\frac{1}{2}}t_s + \gamma_ch_ct_c\frac{E_c}{E_s} \quad (2)$$

where γ_s is a coefficient considering the difference between the arc length and the chord length, which could be assumed as 1.1 based on the numerical analyses; and γ_c is a coefficient considering the concrete compressive area below the steel crest, which could be assumed as 1.4 based on the numerical analyses. Combining the above equations, the ultimate load capacity q_{\max} could be predicted as:

$$q_{\max} = \frac{2[\gamma_s(w^2 + 4h_s^2)^{\frac{1}{2}}t_s + \gamma_ch_ct_c\frac{E_c}{E_s}]f_s}{\alpha_1wD} \quad (3)$$

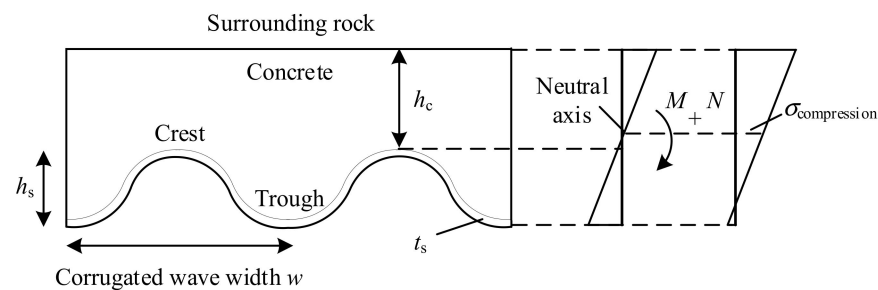


Figure 12. Section stress analysis for the middle top region.

Utilizing Equation (3), the predicted ultimate capacities are also listed in Table 1, noting that the concrete crushing failure is not considered in this method as it should be avoided in design. With an average error of 2.7% and a standard deviation of 4.7%, the proposed analytical method is regarded as suitable for practical design. However, it should be noted that the conclusions are valid within the parameter range considered in this research, while future studies might be required for wider applications.

7. Conclusions

This study presents a novel composite support system known as the corrugated steel–concrete (CSC) structure, which is proposed for use in primary tunnel support. Detailed structural descriptions are furnished, and comparisons with earlier applications are made. Elaborate 3D finite element models were proposed, which were constructed to examine the full elastoplastic response until failure, taking into account the interfacial properties between the steel and concrete, alongside the interactions with its surrounding rock. Parametric analyses were then conducted, encompassing typical design ranges. Subsequently, theoretical analyses were performed, and design equations were proposed, displaying a high degree of efficiency and accuracy. The main findings are as follows:

- (1) An innovative CSC composite structure employed in tunnel support was proposed, accompanied by detailed construction methods. The novel composite structure has high stability performance compared to previous steel structures, since the concrete can provide out-of-plane support. Precise elastoplastic finite element models were developed to assess the mechanical response until the failure of the proposed system. These models additionally account for the steel–concrete interfacial properties and contact interactions. Non-uniform loads were analytically applied based on field methods, with foundation interactions computed through frictionless elements. Under typical loading conditions, cohesive stress and frictional forces provided adequate connections such that the structure behaved in a nearly fully composite way. The

predominant failure modes were steel yield and concrete crushing in the middle top area.

- (2) Parametric analyses spanning common design ranges were conducted, revealing that the thickness of the concrete, thickness of the steel, and height of the corrugated plate were key factors affecting the structural response. Designers ought to avoid excessively thick concrete, which could lead to brittle concrete crushing failure.
- (3) Theoretical analyses were conducted based on numerical studies, from which design equations and recommendations were developed. These demonstrated high efficacy and accuracy for most engineering applications.

The proposed support system is not limited to tunnel support, but can also potentially find broad applications in other underground engineering projects. Further research is necessary to examine more complex geometries, materials, and loading conditions. Future research will encompass lateral test verification, a broader parameter range, various load types, and the effects of connection contact between different modules.

Author Contributions: Conceptualization, C.G.; investigation, Z.Z.; validation, M.W.; visualization, H.Z.; writing—review and editing, Z.W. All authors have read and agreed to the published version of the manuscript.

Funding: This research was funded by the National Key R&D Program of China (Grant No. 2022YFC3800901), the National Natural Science Foundation of China (Grant No. 52278385), and the Beijing Municipal Education Commission (Grant No. KM202210005019).

Institutional Review Board Statement: Not applicable.

Informed Consent Statement: Not applicable.

Data Availability Statement: The data presented in this study are available from the corresponding authors upon reasonable request.

Conflicts of Interest: The authors declare no conflict of interest.

References

1. National Research Council. *Underground Engineering for Sustainable Urban Development*; National Academies Press: Washington, DC, USA, 2013.
2. Curiel-Esparza, J.; Canto-Perello, J.; Calvo, M.A. Establishing sustainable strategies in urban underground engineering. *Sci. Eng. Ethics* **2004**, *10*, 523–530. [[CrossRef](#)] [[PubMed](#)]
3. Galan, I.; Baldermann, A.; Kusterle, W.; Dietzel, M.; Mittermayr, F. Durability of shotcrete for underground support—Review and update. *Constr. Build. Mater.* **2019**, *202*, 465–493. [[CrossRef](#)]
4. Guler, S.; Öker, B.; Akbulut, Z.F. Workability, strength and toughness properties of different types of fiber-reinforced wet-mix shotcrete. *Structures* **2021**, *31*, 781–791. [[CrossRef](#)]
5. Liu, G.; Zhao, J.; Zhang, Z.; Wang, C.; Xu, Q. Mechanical properties and microstructure of shotcrete under high temperature. *Appl. Sci.* **2021**, *11*, 9043. [[CrossRef](#)]
6. Kaufmann, J.; Loser, R.; Winnefeld, F.; Leemann, A. Sulfate resistance and phase composition of shotcrete. *Tunn. Undergr. Sp. Tech.* **2021**, *109*, 103760. [[CrossRef](#)]
7. Yelemessov, K.; Sabirova, L.B.; Martyushev, N.V.; Malozyomov, B.V.; Bakhmagambetova, G.B.; Atanova, O.V. Modeling and Model Verification of the Stress-Strain State of Reinforced Polymer Concrete. *Materials* **2023**, *16*, 9. [[CrossRef](#)] [[PubMed](#)]
8. Siddique, R.; Naik, T.R. Properties of concrete containing scrap-tire rubber—An overview. *Waste Manag.* **2004**, *24*, 563–569. [[CrossRef](#)] [[PubMed](#)]
9. Chen, T.; Su, M.; Pan, C.; Zhang, L.; Wang, H. Local buckling of corrugated steel plates in buried structures. *Thin-Walled Struct.* **2019**, *144*, 106348. [[CrossRef](#)]
10. Zhang, W.; Mahdavian, M.; Yu, C. Lateral strength deflection of cold-formed steel shear walls using corrugated sheathing. *J. Constr. Steel Res.* **2018**, *148*, 399–408. [[CrossRef](#)]
11. Zhang, M.; Han, Y.; Li, P.; Guo, C. Field experimental study on steel-corrugated plate-mold bag concrete supporting structure of circular shaft. *Tunn. Constr.* **2022**, *42*, 1146–1155.
12. Chen, X. *Numerical Simulation and Design Scheme of Assembled Type Corrugated Steel Plate Lining for Subway Tunnel*; Beijing University of Technology: Beijing, China, 2017.
13. Chen, W.; Liu, B.; Liu, R. Analysis of Working Effect of Corrugated Steel Lining on Tunnel Lining Fall. *Tunn. Constr.* **2018**, *12*, 384.

14. Takashi, H. Corrugate Fiber Reinforced Plastic Sheet in Repairing Tunnel Linings. *J. Civil Eng. Architect.* **2015**, *9*, 684–690. [[CrossRef](#)]
15. Korusiewicz, L.; Kunecki, B. Behaviour of the steel box-type culvert during backfilling. *Arch. Civ. Mech. Eng.* **2011**, *11*, 637–650. [[CrossRef](#)]
16. Garcia, D.B.; Moore, I.D. Behavior of coupling band joints in buried corrugated steel pipelines. *J. Geotech. Geoenviron.* **2014**, *140*, 04013014. [[CrossRef](#)]
17. Sezen, H.; Yeau, K.Y.; Fox, P.J. In-situ load testing of corrugated steel pipe-arch culverts. *J. Perform. Constr. Fac.* **2008**, *22*, 245–252. [[CrossRef](#)]
18. Beben, D. Dynamic amplification factors of corrugated steel plate culverts. *Eng. Struct.* **2013**, *46*, 193–204. [[CrossRef](#)]
19. Li, Y.; Xu, J.; Nan, F.; Su, H.; Zhao, T. Dynamic Simulation and Experimental Study of the HDPE Double-Walled Corrugated Pipe Grouting Robot. *Sustainability* **2022**, *14*, 6776. [[CrossRef](#)]
20. Sun, K.; Hong, Y.; Xu, W.; Hou, Z.; Liu, X.; Yu, M.; Yuan, Z. Analysis and prediction of mechanical characteristics of corrugated plate as primary support in tunnels. *Tunn. Undergr. Sp. Tech.* **2021**, *111*, 103845. [[CrossRef](#)]
21. Sun, K.; Hong, Y.; Xu, W.; Liu, H.; Zhen, Y.; Qin, J. Analysis and prediction of the mechanical behavior of corrugated plate as primary support in tunnels with elastoplastic constitution. *Tunn. Undergr. Sp. Tech.* **2022**, *124*, 104451. [[CrossRef](#)]
22. Kunecki, B.; Korusiewicz, L. *Field Test of Soil-Steel Arch with Ribs and Calculation of Internal Forces on the Basis of Measured Strains; Research and Applications in Structural Engineering, Mechanics and Computation*; CRC Press: Boca Raton, FL, USA, 2013; pp. 933–934.
23. Hatami, H.; Shariati, M. Numerical and experimental investigation of SS304L cylindrical shell with cutout under uniaxial cyclic loading. *Iran. J. Sci. Technol. Trans. Mech. Eng.* **2019**, *43*, 139–153. [[CrossRef](#)]
24. Zhang, L.; Hebert, R.; Wright, J.T.; Shukla, A.; Kim, J.H. Dynamic response of corrugated sandwich steel plates with graded cores. *Int. J. Impact. Eng.* **2014**, *65*, 185–194. [[CrossRef](#)]
25. Zamanifar, H.; Sarrami-Foroushani, S.; Azhari, M. Static and dynamic analysis of corrugated-core sandwich plates using finite strip method. *Eng. Struct.* **2019**, *183*, 30–51. [[CrossRef](#)]
26. Guo, Y.T.; Nie, X.; Tao, M.X.; Ding, R.; Tang, L.; Fan, J.S. Selected series method on buckling design of stiffened steel-concrete composite plates. *J. Constr. Steel Res.* **2019**, *161*, 296–308. [[CrossRef](#)]
27. Sokolinsky, V.S.; Indermuehle, K.C.; Hurtado, J.A. Numerical simulation of the crushing process of a corrugated composite plate. *Compos. Part A Appl. Sci. Manuf.* **2011**, *42*, 1119–1126. [[CrossRef](#)]
28. Cheng, Z.; Zhang, Q.; Bao, Y.; Deng, P.; Wei, C.; Li, M. Flexural behavior of corrugated steel-UHPC composite bridge decks. *Eng. Struct.* **2021**, *246*, 113066. [[CrossRef](#)]
29. Guo, Y.T.; Yang, Y.; Song, S.Y.; Fan, J.S. Shear-slip failure in steel-concrete-steel composite beams with bidirectional webs. *Thin-Walled Struct.* **2021**, *164*, 107743. [[CrossRef](#)]
30. Song, S.; Guo, Y.; Fan, J.; Elghazouli, A.Y. Shear Contribution of Flange Dowel Action in Steel-Concrete-Steel Composite Structures. *Thin-Walled Struct.* **2021**, *169*, 108354. [[CrossRef](#)]
31. Guo, Y.T.; Nie, X.; Fan, J.S.; Tao, M.X. Shear resistance of steel-concrete-steel deep beams with bidirectional webs. *Steel Compos. Struct.* **2022**, *42*, 299–313.
32. Abbas, H.S.; Bakar, S.A.; Ahmadi, M.; Haron, Z. Experimental studies on corrugated steel-concrete composite slab. *Gradevinar* **2015**, *67*, 225–233. [[CrossRef](#)]
33. Zhang, J.; Liu, B.; Liu, R. Behavior of sinusoidal-corrugated-steel-plate-concrete composite slabs: Experimental investigation theoretical model development. *J. Constr. Steel Res.* **2021**, *187*, 106958. [[CrossRef](#)]
34. Khanouki, M.A.; Sulong, N.R.; Shariati, M.; Tahir, M.M. Investigation of through beam connection to concrete filled circular steel tube (CFCST) column. *J. Constr. Steel Res.* **2016**, *121*, 144–162. [[CrossRef](#)]
35. Kanchanadevi, A.; Ramanjaneyulu, K.; Gandhi, P. Shear resistance of embedded connection of composite girder with corrugated steel web. *J. Constr. Steel Res.* **2021**, *187*, 106994. [[CrossRef](#)]
36. Sormunen, L.A.; Kalliainen, A.; Kolisoja, P.; Rantsi, R. Combining mineral fractions of recovered MSWI bottom ash: Improvement for utilization in civil engineering structures. *Waste Biomass Valori.* **2017**, *8*, 1467–1478. [[CrossRef](#)]
37. Leblouba, M.; Barakat, S.; Maalej, M.; Al-Toubat, S.; Karzad, A.S. Normalized shear strength of trapezoidal corrugated steel webs: Improved modeling and uncertainty propagation. *Thin-Wall Struct.* **2019**, *137*, 67–80. [[CrossRef](#)]
38. National Railway Administration of the P.R.C. Code for Design of Railway Tunnel. China Railway Publishing House Co., Ltd.: Beijing, China, 2016.
39. CEN European Committee for Standardization. *EN 1994-1-1 Eurocode 4: Design of Composite Steel and Concrete Structures—Part 1-1: General Rules and Rules for Buildings*; British Standards, Ltd.: London, UK, 2004.
40. Code, M. *Fib Model Code for Concrete Structures*; Wilhelm Ernst & Sohn: Berlin, Germany, 2010.
41. Hognestad, E. *Study of Combined Bending and Axial Load in Reinforced Concrete Members*; University of Illinois at Urbana Champaign, College of Engineering, Engineering Experiment Station: Urbana, IL, USA, 1951.
42. DSS (Dassault Systèmes Simulia Corp). *ABAQUS Analysis User's Manual 6.14-2*; DSS: Providence, RI, USA, 2014.
43. Lourenço, P.B. *Computational Strategies for Masonry Structures*; Delft University of Technology: Delft, The Netherlands, 1996.

44. Guo, Y.; Bompa, D.V.; Elghazouli, A.Y. Nonlinear numerical assessments for the in-plane response of historic masonry walls. *Eng. Struct.* **2022**, *268*, 114734. [[CrossRef](#)]
45. Standardization Administration of the P.R.C. *Cold-Formed Corrugated Steel Pipes GB/T 34567-2017*; Standardization Administration of the P.R.C.: Beijing, China, 2017.

Disclaimer/Publisher's Note: The statements, opinions and data contained in all publications are solely those of the individual author(s) and contributor(s) and not of MDPI and/or the editor(s). MDPI and/or the editor(s) disclaim responsibility for any injury to people or property resulting from any ideas, methods, instructions or products referred to in the content.